AN ABSTRACT OF THE THESIS OF

Mario A. Apreotesi for the degree of Honors Baccalaureate of Science in Mechanical Engineering presented on June 2, 2006. Title: Microscale Thermal Management Using Membrane Vapor Extraction

Abstract approved: _____
Deborah V. Pence

With the miniaturization of microelectronics and increase of processor speeds in the last few decades, thermal management is drastically affecting overall packaging and system capabilities. Due to the special needs introduced, research focusing on microscale cooling has increased. This study combines the positive characteristics of single- and two-phase flows in branching microchannels by locally extracting the generated vapor. A test fixture and test flow loop were designed and fabricated with which to experimentally assess the thesis statement of the project. Using water as the working fluid, preliminary data were gathered for inlet flow rates ranging between 2 and 10 g/min and vapor extraction pressure differentials ranging between 14 and 48 kPa. The inlet flow was 2 to 3 ˚C below the saturation temperature (subcooled) with a constant energy input of 8.5 W. In the preliminary tests, vapor was extracted from the two-phase flow. Although the preliminary results indicate the need for further improvements in the test fixture, flow loop and testing procedure, the initial trends support the thesis statement and suggest the need for further testing. After improvements are made, additional data will be collected and correlations will be generated.

Key Words: heat sinks, vapor extraction, membrane, microchannel, two-phase flow
Corresponding e-mail address: apreotem@engr.orst.edu

©Copyright by Mario A. Apreotesi
(June 2, 2006)
All Rights Reserved

Microscale Thermal Management Using Membrane Vapor Extraction

by

Mario A. Apreotesi

A PROJECT

submitted to

Oregon State University

University Honors College

in partial fulfillment of
the requirements for the
degree of

Honors Baccalaureate of Science in Mechanical Engineering (Honors Scholar)

Presented June 2, 2006
Commencement June 2006

Honors Baccalaureate of Science in Mechanical Engineering project of Mario A. Apreotesi presented on June 2, 2006.

APPROVED:

_____

Deborah V. Pence, representing Mechanical Engineering

_____

James Liburdy, representing Mechanical Engineering

_____

Vinod Narayanan, representing Mechanical Engineering

_____

Joe Hendricks, Dean of University Honors College

I understand that my project will become part of the permanent collection of Oregon State University, University Honors College. My signature below authorizes release of my project to any reader upon request.

_____

Mario A. Apreotesi, Author

ACKNOWLEDGEMENTS

I would like to thank Dr. Pence for her patience and help in completing this project and paper. Although she had to explain some things multiple times, she did not give up on me or become overly irritated—I least I hope not. I would also like to thank Dr. James Liburdy and Dr. Vinod Narayanan for their help with different phases of this project. Thanks should also be given to Greg Mouchka for his help with many different aspects of this project, especially the design and fabrication of the test flow loop.

TABLE OF CONTENTS

LIST OF FIGURES

LIST OF TABLES

NOMENCLATURE

Symbols

A	area
AC	constant
B	inverse mean temperature; Bias error
c_p	specific heat
d	diameter
D	diameter
e	error
E	modulus of elasticity
f	frequency
g	gravity constant
h	heat transfer coefficient
H	height
I	current
k	thermal conductivity
K	permeability
L	length
m	polynomial order
$\dot{m}$	mass flow rate
n	number of branches
N	0^{th} level branches; total number of data points
Nu	Nusselt number
p	distributed load pressure
P	pressure; precision error
Pr	Prandtl number
q	heat transferred
$\dot{Q}$	heat transferred
r	radius
s	standard deviation
R	resistance; dependent variable
Ra	Rayleigh number
Re	Reynolds number
S	shape factor
t	time
th	thickness
T	temperature
u	mean velocity; uncertainty
U	heat transfer coefficient
v	Poisson's ratio
V	voltage
$\dot{V}$	volumetric flow rate

w	width
x	thermodynamic quality; independent variable
y	data point

Greek Symbols

α	thermal diffusivity
β	diameter ratio
γ	length ratio
ε	emissivity
μ	dynamic viscosity
ν	kinematic viscosity
ρ	density
σ	Boltzman's constant
ω	deflection

Subscripts

air	air; ambient
al	porous aluminum
bias	bias error
catch	catch system
ch	microchannels
ci	data point
D	diameter
e	developing velocity profile entrance region
f	fluid; saturated fluid
fit	curve fit
fractal	fractal
g	saturated vapor
H	hydraulic
htr	heater
i	inlet
in	inlet
k	branch level
lm	log mean
m	mean
M	number of branch levels
ncv	natural convection
o	out, outer
out	out
pm	porous membrane
peek	PEEK^{TM} material
press	pressure
rad	radiation
s	surface, side

side	side
ss	stainless steel (fractal)
T	thermal
vac	vapor plenum
vap	vapor
x	independent variable

MICROSCALE THERMAL MANAGEMENT USING MEMBRANE VAPOR EXTRACTION

Background

With the emergence of new technological applications in the last few decades, the need for efficient and effective thermal management continues to increase. The greatest needs are arising in microelectronics. With the development of further miniaturization in microelectronics and increased processor speeds, thermal management is drastically affecting overall packaging and system capabilities. The cooling of electronics and other micro-applications is fundamentally different from that of most conventional applications. Not only does the heat need to be removed, but the object needs to be maintained at a low and relatively uniform and stable temperature. Due to the special needs introduced by these new applications, research focusing on such cooling has increased.

The early investigations looked to the conventional cooling process: forced-air convective heat transfer. The size, shape and configuration of electronic modules were investigated to maximize cooling capacity from circuit boards using forced-air convection over the circuit board. Representative studies of forced-air convection cooling include Sparrow et al. [1] investigating the convective heat transfer for air flows in arrays of heat-generating square modules located along one wall of a flat rectangular duct. Jubran et al. [2] furthered such studies by investigating the convective heat transfer of rectangular and cylindrical modules As the microelectronics capabilities continued to

increase along with increasing miniaturization, the heat being generated and needing to be dissipated increased. Soon thereafter, the upper limits of heat transfer coefficients for forced-air convection cooling were reached. Consequently, new methods were considered and investigations into microchannel heat sinks began.

Thermal management in microscale channel geometries is advantageous due to the high surface area per unit volume, the large heat transfer coefficients, small mass and minimal volume. Microchannels are defined as those containing hydraulic diameters ranging nominally between 10 to 200 μm. Initial research and applications centered on single-phase flow through microchannels. Such studies have been abundant since the pioneering investigation of Tuckerman and Pease [3]. In their report, they theoretically proposed that a cooling capacity of 1000 W/cm^2 could be achieved using single-phase flow in microchannel heat sinks. This objective has become the benchmark for microscale cooling capacity. Their experimental setup was optimized to reach a cooling capacity of 790 W/cm^2. Qu and Mudawar [4] continued single-phase studies in microchannels and concluded that the outlet fluid temperature and the temperature of the fluid in the heat sink decrease at the expense of a greater pressure drop across the heat sink. Zhang et al. [5] showed that for single-phase flow in microchannels the pressure drop across the microchannels decreases with increasing input power. This inverse relationship is due to the decrease in the liquid viscosity resulting from the increased temperature. From numerous studies performed, large stream-wise increases in the bulk fluid temperature and heat sink temperature were observed. This inability to maintain a uniform heat sink temperature can lead to uneven thermal expansion of the surrounding materials causing probable changes in the electrical properties of a circuit board. To

compensate for the stream-wise increasing temperature, the flow rates were greatly increased resulting in larger pressure drops. With these conclusions, studies of two-phase flows in microchannels have become increasingly more important in the last few years.

Two-phase boiling microchannel studies offer two advantages over single-phase flow in microchannels: nearly uniform heat sink temperature at the fluid saturation temperature and minimal fluid flow rates for the same cooling load. The conventional layout of microchannels (and heat sinks in general) consists of a series of parallel straight channels, but this often leads to several difficulties. Numerous two-phase boiling microchannel studies have been performed revealing the details of these difficulties. Mertz et al. [6] reported fluctuations and maldistribution of two-phase flow within a parallel series of microchannels. In separate investigations of two-phase pressure drop in parallel microchannels, Qu and Mudawar [7] observed similar phenomena and identified two types of two-phase instability: pressure drop oscillation and parallel channel instability. Pressure drop oscillation produced periodic, large-amplitude flow oscillations, which could trigger dry-out (critical heat flux—CHF). Parallel channel instability produced only mild flow fluctuations resulting in less frequent occurrences of dry-out. Along with dry-out, flow reversal was observed by Steinke and Kandlikar [8] in an investigation of two-phase boiling of water in parallel microchannels. Rapid evaporation of liquid in the contact line region led to dry-out. And with the absence of film on the heated surface, the local surface temperature rapidly increased. In these investigations, dry-out was occasionally observed in entire channels. Similar results were reported by Jiang et al. [9] in studying even smaller microchannels having hydraulic diameters of 26 and 53 μm. In all these investigations, dry-out was followed by

extremely high temperatures leading to electronics failure. Parallel channel instability also produced a non-uniform temperature distribution that could lead to uneven thermal expansion. Temperature gradients along the heated surface can also lead to thermal stresses and mechanical fatigue, especially at the interface between two dissimilar materials.

The investigations of Jiang et al. [9] also reported an appreciable pressure drop increase upon the commencement of boiling in the microchannels. Similar pressure drop increases shortly after the onset of boiling were reported by Zhang et al. [10]. Their studies accounted for this sharp increase by observing that the density of the vapor is much less than that of the liquid leading to a sudden increase in the local volumetric flow rate. The local acceleration of the flow results in the increased pressure drop. Overall, the two-phase studies in parallel microchannels observed greater pressure drop than that in single-phase flow and flow instabilities leading to possible dry-out and/or non-uniform temperature distribution.

To improve the cooling characteristics of single-phase flow in microchannels other studies have been performed by re-evaluating the channel geometry and network arrangement of the channels. Bau [11] demonstrated with mathematical models that the optimization of variable cross-sectional microchannels reduced the maximal temperature and minimized temperature gradients along the length of the channel. Reduction of the surface temperature resulted from tapering the channel in the stream-wise direction. However, this decrease in the stream-wise channel diameter led to an increased velocity and hence increased the pressure drop and pumping power required. Ideally, it is desirable to achieve similar surface temperature distributions without an increased

pressure drop. Recently, breakthroughs have been made to implement the same fractal-like flow networks used by natural and biological processes to overcome high pressure drops in microchannel flows. Representative examples of fractal-like channel structures are the circulatory system of the human body and root systems found in plants. As either stretches out from its source, the hydraulic diameter slowly decreases as it branches in to more and more 'sub channels' resulting in an increase of the flow area. Following proposals made by West et al. [12] fractal-like networks have been engineered with fixed diameter and length scale ratios between consecutive branching levels. Pence [13] first proposed that this geometric layout of the channels, along with helping to reduce the pressure drop, ensures an even distribution of the flow and surface wall temperature. Later studies by Pence [14] validated those proposals by comparing heat sinks with this fractal-like flow network to those with the conventional parallel channel array. The maximum channel wall temperature and the total pressure drop across a heat sink were the characteristics of interest. The studies concluded that similar maximum wall temperatures and total pressure drop across the heat sink were obtained with a fifty percent less density for the fractal-like network—the fractal-like network provided superior results. In another study, Pence and Enfield [15] defined benefit-to-cost ratio as the quotient of the advected energy dispelled from a surface and of the flow power. Heat sinks with fractal-like branching networks and parallel channel networks were compared and it was shown that fractal-like networks have a greater benefit-to-cost ratio. The fractal network design improves the performance of microchannels in single-phase flows and is anticipated to enhance two-phase flows as well.

Studies have been done to model single-phase and two-phase pressure drops across fractal-like flow networks. Similar to conventional network geometries, results show that pressure drops are substantially greater in two-phase flows as a result of vapor formation and acceleration. Despite the fact that the higher pressure drops anticipated in two-phase flow make the use of two-phase microchannels less desirable than single-phase flows, the latent energy exchange is required for high heat flux applications to ensure a uniform temperature distribution. Investigations of Qu and Mudawar [16] using water in parallel microchannels demonstrated that the heat transfer coefficient in two-phase flow decreases with increasing thermodynamic quality and increases with increasing mass velocity. Several inconclusive explanations have been proposed to explain the decrease in heat transfer coefficient with increasing quality. This inverse relationship between the heat transfer coefficient and the fluid quality is central to this project and has been validated by other investigations. Steinke and Kandlikar [8], also using water as the working fluid, reported very large values for the heat transfer coefficient in the low quality region with a sharp decline in the coefficient values as the quality increased. Refrigerant studies performed by Yen et al. [17] observed similar heat transfer coefficient characteristics in microchannel tubes. One of the objectives of this thesis project is to utilize the large heat transfer coefficient values in the low quality region.

Recently studies have been performed evaluating the performance of convective boiling using a porous surface coating. The first investigations evaluated the effect of porous surface in pool boiling applications and showed remarkable improvements in heat transfer coefficients and critical heat flux. Subsequent studies examined internal porous

coatings on flow boiling. Ikeuchi et al. [18] plated the internal surface of a 17.05 mm diameter tube with 0.115 mm diameter copper particles. Heat transfer coefficient values improved by approximately five times. Ammerman and You [19] investigated the performance of surface coating in square minichannels and reported similar heat transfer improvements. The use of porous membranes in this thesis project is expected to replicate this characteristic of porous surface coatings and help improve heat transfer characteristics.

This thesis project focuses on utilizing the large heat transfer coefficient of two-phase flows in the low-quality region by extracting, through a porous hydrophobic membrane, vapor from the fractal-like microchannel network. The vapor is removed where it is formed, rather than having to be pushed through the entire flow network, which ultimately reduces the pressure drop across the heat sink to values similar to those achieved with single-phase flows. Simply, the objective is to combine the positive characteristics of both two-phase and single-phase flows. The extraction of vapor utilizing a relatively small pressure differential across a membrane from two-phase flows in branching microchannel heat sinks should maintain the high heat flux capabilities of two-phase flows, but with a reduced stream-wise (radial) pressure drop. This idea has the added benefit of being useful in situations of low gravity. As gravity is no longer required to separate the vapor from the liquid phase, this application would be feasible in any spatial orientation. The thesis project focused on designing and developing a test fixture and test flow loop, gathering preliminary data, and establishing the viability of these objectives.

Design Requirements

To assess the thesis statement, experiments are needed to collect and analyze data. Experimental measurements are first collected of vapor extraction as a function of applied heat flux, controlled flow rates of water, and regulated vacuum pressure. The data are then reduced and reported. Correlations will be developed to aid designers in formulating branching microchannel heat sinks particular to their application. However, before performing experiments and collecting data, a fixture and flow loop needed to be designed and fabricated. The test fixture and test loop designs are required to validate the thesis statement.

The first step is to identify the data required to investigate the effect of extracting vapor from two-phase flow in branching microchannels. Mass flow rate, temperature and pressure measurements at the inlet plenum and exit plenums of the fixture are required. Knowledge of the mass flow rates allows calculation of the percentage of the flow extracted as vapor. The exit fluids include the liquid that exits the fractal, the extracted vapor and the non-extracted vapor that passes through the fractal. Controlling the inlet mass flow rate and applying conservation of mass, only two of the three exit flow rates are required. The inlet flow rate is regulated to not remain in the operating range. Measurement of the temperature and pressure identifies the state of the fluid in the inlet plenum, vapor plenum, exit plenum and within the microchannels. The fixture design should accommodate accurate and precise temperature and pressure measurements. Figure 1 provides a general layout of the test fixture mainly detailing where the temperature, pressure and flow rate should be measured. This entails acquiring the data

relatively close to each port without disrupting the flow and possibly triggering turbulent conditions.

Secondly, the flow needs to transition to two-phase flow while within the microchannels to test the hypothesis. The fluid is preheated in the flow loop and brought to within a few degrees of its boiling point. To induce two-phase flow inside the microchannels, heat is provided by a heating block. The amount of vapor generated is a function of the flow rate through the channels, heat supplied to the microchannel flow and inlet temperature of the fluid. Consequently, it is required that the flow rate also be regulated.

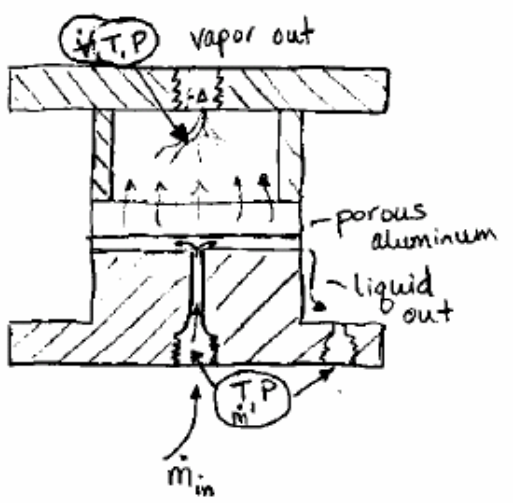

Figure 1: Schematic showing a general design for the test fixture. The measurements that need to be found at certain points are indicated by arrows.

Thirdly, vapor must be extracted from the channels and leaks cannot occur. A hydrophobic porous membrane through which vapor molecules can pass but fluid molecules cannot forms the top surface of the channels. A porous aluminum block provides rigidity to the membrane. The membrane should provide a sufficient seal, which is not possible with solely the porous aluminum. However, the combination of the two porous materials increases the pressure difference required to extract the vapor. A pump is used to overcome this pressure difference to facilitate the extraction of vapor from the microchannels.

There are other design requirements for the fixture and test loop. For example, the fixture should be thermally isolated to simplify the thermodynamic analysis. This is

done by insulating the fixture. The test loop should be interchangeable with similar experiments currently being performed and those planned for the future. The materials used should be resilient to withstand many experiments. The test loop shares some common instrumentation with another flow loop. The integration of this test loop into the existing test loop should allow for an easy transition from one loop to the other. Since the working fluid of the existing test loop is ammonia, it is important that before transitions are made from one test loop to the other that the common elements of the loop can be flushed. The test loop is also required to provide pressurized flow to the fixture and to facilitate the measurements discussed earlier. Obviously, this is not an exhaustive discussion of the design requirements for the fixture and flow loop, but it addresses the main requirements. Other requirements arose as the design progressed, but the awareness of the requirements discussed helped to direct the process of designing the test fixture and test loop.

Design Specifications

From the general design requirements, characteristics of the test fixture and flow loop can be specified. The microchannel fractal element, shown in Fig. 2, is the central part of this project and extraction of vapor is the primary objective. They act as the starting blocks for the design of both the fixture and flow loop. This limits creativity in the possible design solutions, but also helps initialize the approach to satisfy each design requirement. More detailed information regarding the fractal channel network design is given in the following section.

The first design requirement is to measure the temperature, pressure and mass flow rate at the desired locations. The temperature and pressure calculations identify the thermodynamic state of the fluid at a given location, while the flow rate and energy input permit thermodynamic analysis. Accurate measurements are obtained by integrating their collection into the design of the fixture and loop. Although collecting temperature and pressure measurements within the fixture requires greater design specifications, it is imperative to maximize the accuracy of the results. The inlet and extracted vapor temperature and pressure are measured in the test fixture, while the state of the exit fluid is identified just outside the test fixture in the test loop. The inlet properties are found by tapping two small channels perpendicular to the inlet flow stream. A thermocouple and a pressure transducer are placed at the end of each channel. Accurate measurements are

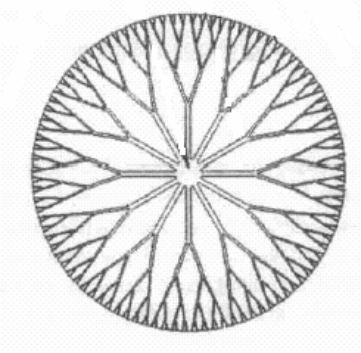

Figure 2: The microchannel fractal element used in the thesis project.

recorded in this manner because the channels are placed immediately before the microchannels. Disruption of the flow is also avoided by not placing the probes directly in the flow. A schematic of the side ports used to measure the properties of the inlet stream is given in Fig. 3. The properties of the extracted vapor are found by placing the probes inside the vapor plenum as detailed in Fig. 4.

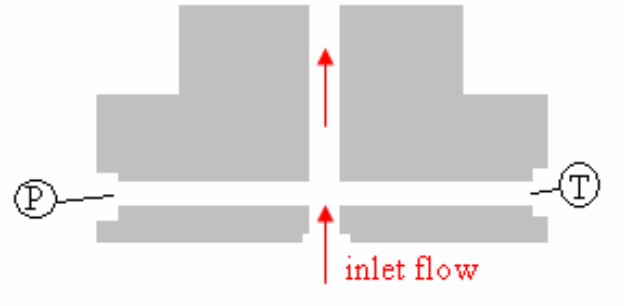

Figure 3: Sketch of the approach used to measure the temperature and pressure of the inlet flow.

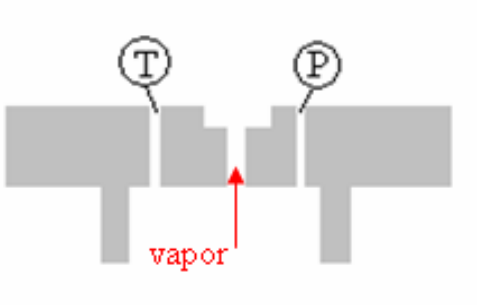

Figure 4: Sketch of how the temperature and pressure of the extracted vapor are measured.

The state of the exit liquid is found by placing the temperature probe in the exit plenum and the pressure transducer immediately outside of the exit port. The mass flow rate of the inlet flow and exit fluid flow are measured using flow meters in the test loop. The flow rate of the extracted vapor is measured by condensing the vapor in a cold bath and then catching it in a bottle placed on a scale. The change in mass over time represents the extracted vapor mass flow rate.

The second design requirement is to create vapor in the fractal microchannels. The fluid is first preheated in the test loop to within 2-3˚ C of its saturation temperature. Compensations are made to allow for varying mass flow rates, operating pressure, and minimal heat loss between the hot oil bath and the test fixture. The flow is then heated to saturation within the microchannels using a block heater. In these two processes, an

important variable is the inlet flow rate for which a nominal value is calculated later in this section.

The inlet stream is preheated by placing part of the test loop in a heating bath filled with oil. The temperature range of the bath is 12 to 200˚ C. Aluminum tubing (0.635 cm OD) is placed in the hot oil bath because it is easy to bend into a coil shape. A heat transfer analysis was performed to identify the length of tubing required in the hot oil bath. Several assumptions were made in this analysis: the free stream temperature of the oil is constant and the velocity profile is not fully developed and the flow is laminar. The flow is shown to have an undeveloped velocity profile in Appendix A. The latter is consequently proven by establishing the mass flow rate of the water to be on the order of 4 g/min. A flow rate of 15 g/min, however, is used in these calculations because it is the upper limit of possible flow rates used in this experiment. The equation governing the heat transferred from a constant-temperature external fluid (the hot oil) to a flow in a tube is given by Eq. 1

$$q = \overline{U} A_s \Delta T_{lm} \tag{1}$$

where $\overline{U}$ is the average overall heat transfer coefficient, A_s is the surface area of the tube submerged in the hot oil bath ($\pi d_o L$), and ΔT_{lm} is the log-mean temperature difference. A schematic of the heat transfer problem is provided in Fig. 5 identifying the location of properties. The log-mean temperature difference is the average of the temperature difference over the tube length and is defined as

$$\Delta T_{lm} = \frac{\Delta T_o - \Delta T_i}{\ln(\Delta T_o / \Delta T_i)} \tag{2}$$

where $\Delta T_o = T_\infty - T_{m,o}$

$\Delta T_i = T_\infty - T_{m,i}$

For the entire tube, the heat transferred to the fluid can also be expressed as

$$q = \dot{m} c_p (T_{m,o} - T_{m,i}) \tag{3}$$

where $\dot{m}$ is the mass flow rate of water and c_p is the specific heat of water evaluated at the average mean temperature along the tube. Setting Eqs. 1 and 3 equal to each other and solving for L, the required length of tube as a function of U is

$$L = \frac{\dot{m} c_p (T_{m,o} - T_{m,i})}{\overline{U} \pi d_o \Delta T_{lm}} \tag{4}$$

The average heat transfer coefficient, U, is found using a Nusselt number correlation developed by Sieder and Tate [20] and is of the form

$$\overline{Nu}_D = 1.86 \left(\frac{\mathrm{Re}_D \, \mathrm{Pr}}{L/D} \right)^{1/3} \left(\frac{\mu}{\mu_s} \right)^{0.14} \tag{5}$$

where all properties except μ_s (s represents

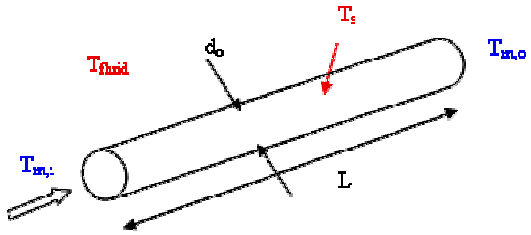

Figure 5: Schematic of heat transfer analysis for aluminum tube in hot oil bath.

surface) are evaluated at the mean temperature of the fluid: $\overline{T}_m \equiv (T_{m,i} + T_{m,0})/2$. The Nusselt number is defined as

$$\overline{Nu}_D = \frac{\overline{U} d_o}{k_f} \tag{6}$$

where k_f is the thermal conductivity of water evaluated at the mean temperature. As stated earlier, the length of the tube needed is a function of U, but in Eqs. 5 and 6 it is also observed that U is a function of L. Iterative calculations must be performed to find the length of tube needed. The property values and the iterative calculations are detailed in Appendix A. While the required length of the tube is found to be approximately 5.1 cm for a bath temperature of 175 ˚C, the amount of submerged tube was increased to 30 cm. This ensures that the fluid reaches the desired preheating temperature and allows for a lower bath temperature. Adjustments for varying mass flow rate and operating temperature are easily made by varying the temperature of the hot oil bath. The temperature of the hot oil bath for varying inlet mass flow rates is also provided in Appendix A. The tubing between the hot oil bath and the test fixture is insulated to minimize heat loss. In this manner, the inlet flow is preheated to within 2-3˚ C of its saturation temperature.

To heat the flow inside the microchannels, coiled Nichrome-80 wire is embedded in the porous aluminum to act as a block heater. Figure 3.C (in Appendix C) shows the block heater apparatus with the coiled wire embedded in the circular path. Initially, a non-porous heating pad placed below the fractal-network piece was considered but it is not feasible because wires inserted into it create a small bulge. This bulge is not uniform in size making it very difficult to model and manufacture the surrounding parts to create a

tight seal. Embedding the coiled wire in the porous aluminum avoids this problem. Thermally conductive paste is placed within the groove and surrounds the heating coil to maximize the transfer of heat from the wire to the heating block. The paste also electrically insulates the coiled wire. The generated power (or energy input) of the heating block is given by

$$\dot{q}_{htr} = I^2 R \tag{7}$$

where I is the current in the coil and R is the resistance of the coil. To determine the percentage of heat transferred to the microchannels, an electric circuit analogy is used as an approximation and is detailed in Fig. 6.

The thermal resistance equivalent can be calculated as

$$R_T = L/kA \tag{8a}$$
$$R_T = 1/Sk \tag{8b}$$
$$R_T = 1/hA \tag{8c}$$

where k is thermal conductivity of the medium, A is the cross-sectional area, L is the distance through the medium and S is the shape factor for two-dimensional conduction. Details of this approximation are provided in Appendix A where it is shown that approximately 1 W of the generated heat is lost to the surroundings and the remainder is transferred through the porous aluminum, hydrophobic membrane and fractal to the flow in the microchannels.

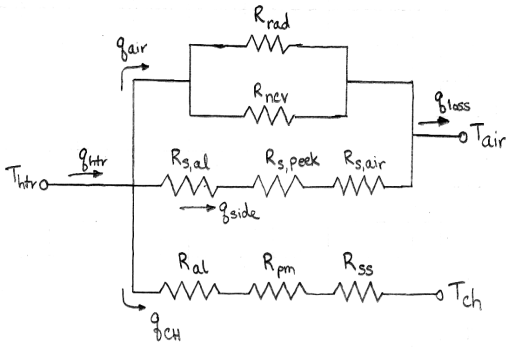

Figure 6: Thermal resistance schematic approximating transfer of heat from coiled wire.

The inlet mass flow rate is determined by a thermodynamic analysis of the system. It was first assumed that 30 W is supplied to the flow in the microchannels. As stated, the inlet flow is preheated to a few degrees below its saturation temperature.

Within the fractal, the flow is heated the remaining few degrees and boiling begins. An exit quality ranging between 0.2 and 0.4 is desired to avoid complete phase transformation of the flow. The thermodynamic equation for evaluating the microchannel flow is

$$\dot{q} = \dot{m}\left[c_p\left(T_f - T_{in}\right) + \left(h_{out} - h_f\right)\right] \tag{9}$$

where $h_{out} = (1 - x_{out})h_f + x_{out}h_g$

where $\dot{q}$ is the supplied power of 30 W, c_p is the specific heat of water or 4.22 kJ/(kg K), T_{in} is the inlet temperature, T_f is the saturation or boiling temperature, h_f is the saturation liquid enthalpy, h_{out} is the exit enthalpy evaluated at differing exit qualities (x_{out}), h_g is the saturation vapor enthalpy and $\dot{m}$ is the inlet flow rate. The first part of Eq. 9 represents the sensible heat required to raise the flow a few degrees to its saturation temperature. The second part is the latent heat required to vaporize the flow and raise its quality. The T-S diagram of the heating process found in Fig. 7 further explains the heating process of the fluid where the blue line represents the vapor dome of water. A conservative assumption of 3˚ C is made for the temperature difference. The inlet mass flow rate is calculated for a range of inlet pressures. It is later shown that the inlet gage pressure is approximately 21 kPa (3 psi). The boiling point at this pressure is 105.3˚ C. The inlet mass flow rate should range between 2 g/min (x = 0.4) and 4 g/min (x = 0.2). In this calculation, the effect of extracting the vapor from the flow is neglected. The range of flow rates tested in the experiments reflects the heating analysis performed here.

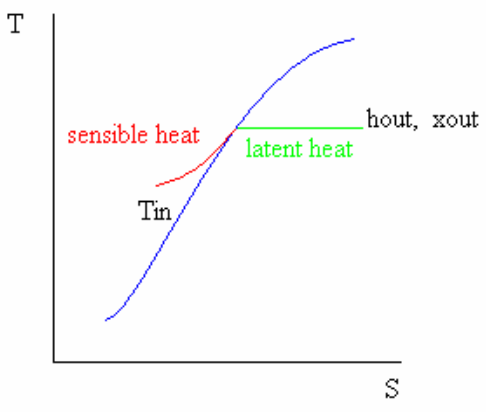

Figure 7: T-S diagram detailing the heat needed to boil the inlet flow stream.

The third design requirement is to extract the vapor. Vapor extraction is not possible without a pressure difference between the microchannels and the vapor plenum. A pressure potential is also required to drive the flow through the test loop and test fixture. Two possibilities were considered to accomplish these objectives. The first was to place the exit plenum under vacuum and have the inlet at atmospheric pressure. However, a high amount of sealing is needed to effectively operate under vacuum, which decreases the tolerances of the design of the fixture and increases its cost. Another drawback is that a vacuum would be needed at the other exits increasing the number of vacuum pumps needed. If the inlet flow is pressurized, only one vapor pump is needed (for vapor extraction). Pressurizing the inlet increases the saturation temperature a few degrees (~ 5–10 ˚C), but porous aluminum has an upper temperature limit of 210 ˚C and the plastics being used are of the same order. The thermodynamic analysis of the vapor extraction (refer to Eq. 9) revealed that pressurizing the flow allows a slightly higher amount of vapor to be extracted. These facts led to the decision to pressurize the inlet flow.

A vacuum pump was placed on the vapor extraction side of the fixture to create the required pressure potential. The pressure differential is governed by Darcy flow and is proportional to the material thickness, L,

$$\Delta P = \frac{\rho \upsilon u}{K} L \tag{10}$$

where ρ is the density of the fluid, ν is the kinematic viscosity of the fluid, u is the mean velocity of the vapor through the porous material (flow rate over cross sectional area) and K is the permeability of the porous material. Metapor HD210—porous aluminum—has a permeability of $2.852 * 10^{-13}$ m^2 (provided by the manufacturer). The density of vapor at

these conditions is 0.5486 kg/m^3, while the kinematic viscosity is 2.443 * 10^{-5} m^2/s. The vapor created is found by multiplying the quality by the inlet mass flow rate as discussed earlier; the maximum theoretical mass flow rate of the vapor is 0.8 g/min or 0.0245 m/s for the 3.556 cm (1.4") diameter cross section of the fractal, membrane and porous aluminum. In this project, it is optimal to minimize the thickness of the porous aluminum. The spiral wire is embedded a 3.2 mm (1/8") into the porous aluminum and to ensure its structural integrity the thickness is set at a quarter inch. Verification of its integrity is detailed in the following paragraph. With these conditions, Eq. 10 states that the pressure differential required to extract the vapor is 7 kPa (1.1 psi). The needed potential is expected to be slightly greater due to the hydrophobic membrane.

The test fixture was clamped to ensure minimal leaking. Deflection of the layers should be minimized to avoid leaking. The most susceptible layer to such deflection is the porous aluminum because it has the smallest thickness. A uniform distributed clamping load of 69 kPa (10 psi) is applied to the edge of the porous aluminum. The load is applied by tightening the six bolts along the perimeter of the test fixture and measured using a torque wrench. The greatest deflection occurs at the center of the layer and is calculated as a function of the applied distributed load pressure *p*, the radius *r* of the layer, its thickness *th*, the material's modulus of elasticity *E* and Poisson's ratio *v* for the material:

$$\omega_{\max} = \frac{3pr^4(1-v^2)}{16E(th)^3} \tag{11}$$

Metapor HD210 has a modulus of elasticity of 10.8 GPa and a Poisson's ratio of 0.33. The deflection at the center of the porous aluminum with a 0.635 cm (0.25 in.) thickness is 0.42 μm (1.64 * 10^{-5} in.). In comparison, the thickness of the hydrophobic membrane

is 0.45 μm and so two membranes will be used ensure that leaks do not occur due to deflection in the fractal piece.

Another important decision is determining the materials of the test fixture parts. The compositions of the fractal and the porous aluminum layer have already been decided. However, the other pieces may be made of a variety of materials. The material used in the main layers of the fixture is vital to thermally isolate the system, prevent leaks and endure repetitive use. Based on these required characteristics, use of plastic, the type of which is justified later, was decided. The plastics layers include the clamp, top and bottom layers shown in Fig. 8 and in Figs. 1.C, 2.C, and 4.C of Appendix C, respectively. The thermal conductivity of the top and bottom layers need to be very small compared to that of porous aluminum and steel to minimize heat transfer to these layers. In general, plastics have relatively small thermal conductivity values. To prevent leaks, plastic with a large elastic modulus needs to be selected to withstand deformation from the applied clamping force. An elastic modulus or ultimate tensile strength on the same order of porous aluminum is sufficient because these layers are thicker than the porous aluminum. The wear factor of the plastic, also, needs to be low enough to withstand continuous testing and use. The wear factor is defined as a material's resistance to wear under high pressure and high

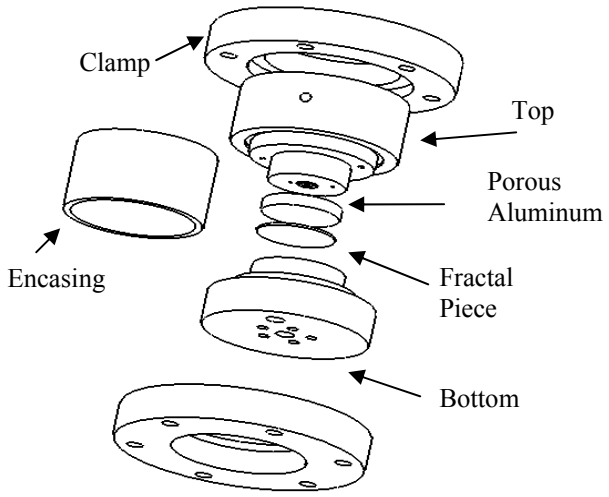

Figure 8: Exploded view of test fixture assembly with the parts labeled.

velocity flow conditions. A low wear factor indicates that a material will withstand such testing conditions and is desired. Three materials were identified as possibilities for these layers: Delrin®, Teflon® and PEEK™ plastics. The ultimate tensile strength of these plastics, respectively, is 125 MPa, 20.7 MPa, and 200 MPa. Their respective wear factor values are 200, 320, and 160. In comparison, the ultimate tensile strength of common steel and rubber are on the order of 800 MPa and 15 MPa, respectively. These two characteristics indicate that PEEK™ is the optimal material to use for each layer. PEEK™ is chosen as the material for the top and bottom layers. However, PEEK™ is extremely expensive so Delrin® plastic is used for the clamp layers.

This is not a comprehensive discussion of the design specifications for the test fixture and test loop. Appropriate o-ring material and sizes needed to be selected. The o-ring grooves needed to be designed to promote effective application of the o-rings. The integration of the test loop into an existing test loop to minimize equipment needs is another list of details. The final design of the test fixture and flow loop are provided in the Appendices B and C with detail drawings of the test fixture parts, pictures of the completed assembly, and a few pictures of the actual test loop.

Experimental Apparatus and Procedure

A schematic of the open-loop test facility used for the thesis project is shown in Fig. 9. The forty gallon bladder tank is filled by pumping water in from the water supply. Once the bladder tank is sufficiently filled, the shut-off valve before the bladder tank is closed. The bladder tank is pressurized by the surge tank, which ensures that fluctuations in the building air supply have a negligible effect on the flow rate and a constant air pressure is supplied to the bladder tank. Fluid passes from the bladder tank through a 15-micron filter. The inlet fluid flow rate is measured with a flow meter and is regulated by a needle valve in the inlet line. The fluid temperature and pressure are read before preheating occurs. As mentioned earlier, the fluid is preheated in a hot oil reservoir. The temperature and pressure of the inlet flow are measured immediately upstream of the microchannel inlet within the test fixture (refer to Fig. 3).

A vapor vacuum pump creates the needed pressure differential to extract vapor from the two-phase flow in the microchannels through the porous media. The temperature and pressure of the extracted vapor are measured in the vapor plenum of the fixture (see Fig. 4). A constant cold water temperature bath condenses the vapor and then it is collected. Calculations are provided in Appendix A verifying that the extracted vapor is completely condensed in the bath. The collected vapor sets on a scale and the flow rate is measured by evaluating the change in mass over time. The vacuum pump is connected to the collector, but does not draw the condensed fluid.

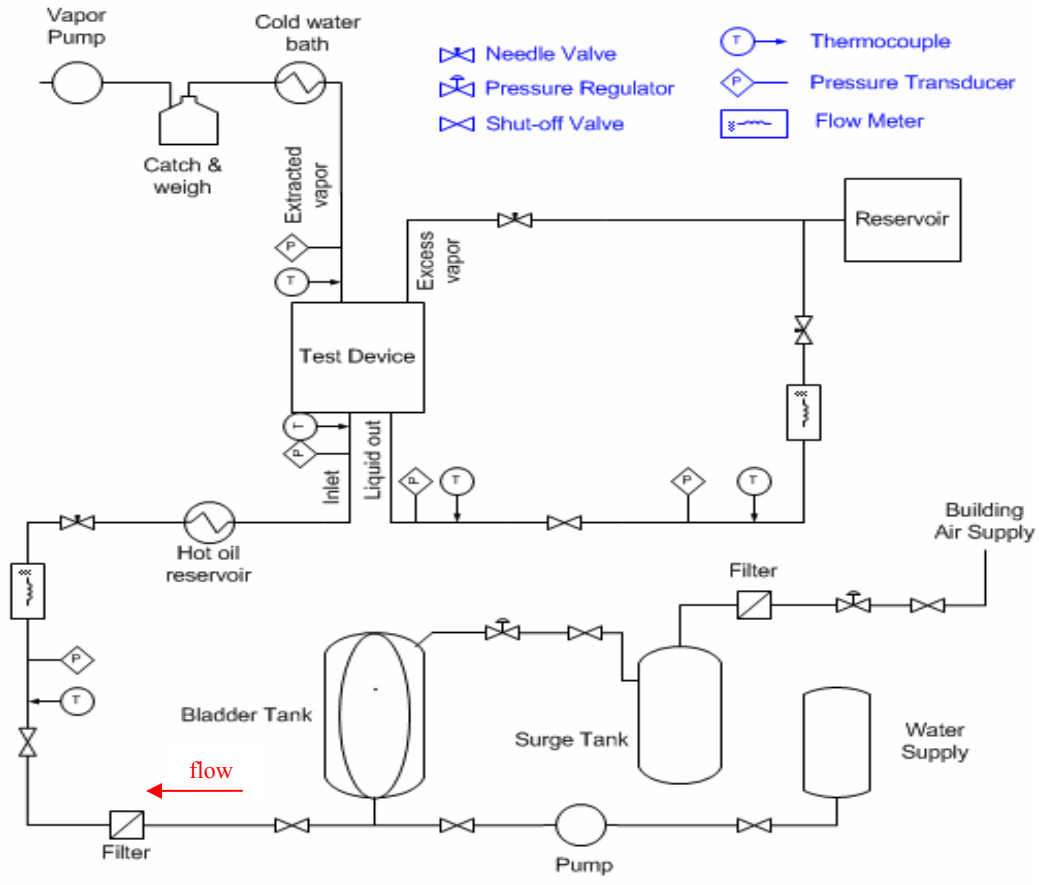

Figure 9: Schematic representing the layout of the test loop for the thesis project.

The two-phase fluid that passes through the microchannels is driven by the pressure difference between the inlet flow and ambient pressure. Needle valves regulate the exit liquid and excess exit vapor flow rates and keep the test fixture pressurized. The temperature of the exit liquid is measured in the exit plenum of the fixture and the pressure is measured directly outside the fixture. A downstream flow meter measures the liquid flow rate. The exit liquid and vapor not extracted are collected in a downstream container.

Description of microchannel fractal network

The fractal microchannel network is shown in Fig. 2 and a more detailed schematic of a set of branching levels is shown in Fig. 10. Its design is characterized by the following scaling laws [14]**:**

$$\beta = \frac{d_{H,k+1}}{d_{H,k}} = n^{-1/AC} \tag{12}$$

$$\gamma = \frac{L_{k+1}}{L_k} = n^{-1/D} \tag{13}$$

$$N_M = n^M \tag{14}$$

The symbols γ and β represent the branching length and diameter ratios, respectively, M is the total number of branching levels not including the 0^{th} level, n is the number of branches from a single channel, D is the Euclidean dimension, $d_{H,k}$ and L_k are, respectively, the hydraulic diameter and length of the channel in level k, and N is the number of 0^{th}-level channels. The index k numbers from zero to M. For the two-dimensional heat sink used in this study, D = 2, n = 2, and AC = 3.

The channel depth remains constant throughout the fractal network and N = 12. The fractal network used has four branching levels (M = 4). With these values, the diameter ratio and length ratio are 0.7937 and 0.7071, respectively. Given a fixed channel depth, the hydraulic diameter is given by the following relationship:

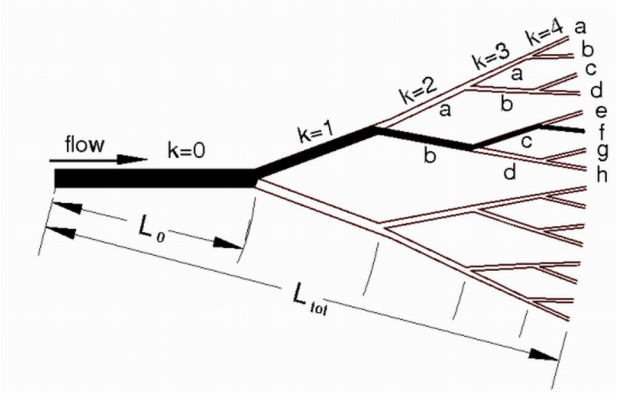

Figure 10: Representation of a subset of the fractal network showing the different branch levels [21].

$$d_H = \frac{4(w_k * H_k)}{2(w_k + H_k)} \tag{15}$$

Table 1 details the specifications of the fractal network which has a total length of 17.5 mm (0.689 in). The diameter of the heat sink is 3.556 cm (1.4 in).

Table 1: Channel dimensions of fractal network (see Figs. 2 and 10)

k	H_k (mm)	w_k (mm)	$d_{H,k}$ (mm)	L_k (mm)
0	0.250	0.643	0.360	6.23
1	0.250	0.333	0.286	4.40
2	0.250	0.204	0.227	3.11
3	0.250	0.141	0.180	2.20
4	0.250	0.100	0.143	1.56

Test Procedure

Water is pumped into the bladder tank with the shut-off valve downstream from the bladder tank closed and the two shut-off valves upstream open. Once sufficiently filled, the first two shut-off valves between the bladder and water supply tanks are closed. The bladder tank is pressurized by the surge tank so that the inlet pressure is 239 kPa (20 psig). The shut-off valve immediately downstream from the bladder tank is opened with the first needle valve completely closed. The needle valve is opened until the desired flow rate is reached. In the preliminary data collection, the flow rate of extracted vapor is measured as a function of inlet liquid flow rate and pressure differential across the porous media. To measure the vapor extraction as a function of inlet flow rate, inlet flow rates ranging between 2 and 10 g/min are evaluated. The inlet flow rate range is determined by using Eq. 9 with the input energy equal to 8.5 W (maximum output of current heater design) and the flow 2˚ C below its saturation temperature. The upper bound is found to be 18 g/min with minimum exit quality assumed to be 0.01. The lower bound is 0.25

g/min corresponding to a maximum exit quality of 0.9. The vacuum provided by the vapor pump results in a pressure differential across the porous media ranging between 14 and 48 kPa (2 - 7 psi). The lower bound of this range is set by atmospheric conditions and the higher bound corresponds to the operating limits of the vapor pump. In all these observations, the temperature of the hot oil reservoir is adjusted so that the inlet is 2˚ C below the saturation temperature. Saturation temperature is identified using the pressure reading at the inlet. LabVIEW is used to monitor and record the measurements of the flow meters, thermocouples and pressure transducers. The recorded data includes the mass flow rate, temperature and pressure for the inlet, extracted vapor and excess liquid flows, and the voltage and current applied to the heater.

Data Reduction and Analysis

To assess the thesis statement, the mass flow rate of extracted vapor is measured as a function of inlet flow rate, input energy and pressure differential across the porous media. The inlet flow rate is measured directly by the mass flow meter. The input energy is determined by the following relationship

$$\dot{Q} = I^2 R_{htr} - \dot{Q}_{loss} \tag{16}$$

where I is the current passing through the wire, R_{htr} is the resistance of the coiled wire and $\dot{Q}_{loss}$ is the heat lost to the environment, which is shown to be 1 W in Appendix A for the conditions evaluated. The vacuum pressure used to extract vapor from the microchannels is calculated as an average pressure drop across the porous media by

$$\Delta P_{vap} = \frac{P_{in} + P_{out}}{2} - P_{vac} \tag{17}$$

where P_{in} is the inlet pressure, P_{out} is the pressure in the exit plenum and P_{vac} is the pressure in the vapor plenum (or vacuum pressure). The mass flow rate of the extracted vapor, following condensation, is calculated as

$$\dot{m}_{vap} = \frac{\Delta m_{catch}}{\Delta t} \tag{18}$$

where m_{catch} is the mass of water inside the catch container and t is time.

Calibration

The measurement instrumentations require calibration in order to record the true outputs. Most of the instruments used in the test loop have been previously calibrated

and integrated into the test loop, with the exception of one pressure transducer. This transducer has a gage pressure range of 0 – 4.138 bar (60 psi). The pressure transducer was calibrated using a pressure chamber with several ports. Air was connected to one port and the pressure was regulated by a pressure regulator. The transducer and a NIST pressure standard were connected to two other ports. The voltage output of the pressure transducer was recorded as a function of absolute pressure indicated by the standard. Data points were collected and the calibration curve was plotted using Excel. The data points were taken in the lower half of the transducer's range because the pressure of the exit plenum will not exceed 240 kPa (35 psi). Using regression analysis in Excel, the calibration curve is determined and is shown in Fig. 11 where P_{out} is the absolute pressure in kPa and V_{out} is the voltage input from the transducer. The standard error for the curve fit is determined by

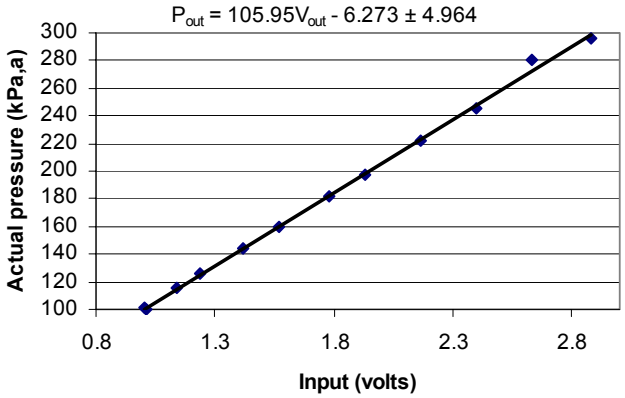

Figure 11: Calibration data points and curve fit for a pressure transducer.

$$e_{fit} = \sqrt{\frac{\sum_{i=1}^{N}(y_i - y_{ci})^2}{v}} \tag{19}$$

$$v = N - (m+1) \tag{19a}$$

where m is the order of the polynomial curve fit, y_i is the i^{th} data point, y_{ci} is the value predicted by the polynomial fit, N is the total number of data points and v represents the degrees of freedom. A first order (linear) curve fit is used so m is equal to 1. The standard error for the fit is multiplied by the t-statistic value tabulated for a ninety-five

percent probability at v. The curve fit error is found to be ± 4.964 kPa (0.72 psi). The bias error of the NIST standard is reported by the manufacturer to be 0.05% of its full scale pressure—689 kPa (100 psi). This corresponds to a bias error of 0.345 kPa (0.05 psi) and the overall calibration error of the pressure transducer is then the root sum square of the curve fit and bias errors;

$$e_{press} = \sqrt{e_{fit}^2 + e_{bias}^2} \tag{20}$$

The calibration error is found to be ± 4.977 kPa (0.722 psi). The outlet pressure is expected to average 103 kPa (15 psi) so the calibration error is approximately 4.8%. Similar calibration procedures were previously performed to the existing pressure transducers, thermocouples and mass flow meters present in the test loop. A table of calibration conversion equations, the associated uncertainty, and measurement ranges are reported in Appendix D for each measurement device.

Uncertainty of Results

The uncertainty for the preliminary results was calculated using the Kline-McClintock method. The uncertainty for each independent variable is calculated using

$$u_x = \sqrt{B_x^2 + \left(t_{v,95} P_x\right)^2} \tag{21}$$

where B is the calibration error (root sum square sum of the bias and curve fit errors for the measurement device as calculated in Eq. 20), $t_{v,95}$ is the student-t factor for a 95% confidence where v is equal to the number of data points minus one, and P is the precision error. The precision error is calculated as

$$P_x = \frac{s_x}{\sqrt{N}} \tag{22}$$

where s is the standard deviation of the data set. The calibration error for each measurement device is given in Table 1.D of Appendix D. The propagation of the independent variable uncertainty values to the dependent variables is defined as

$$u_R = \sqrt{\sum_{i=1}^{n}\left(\frac{\partial R}{\partial x_i}u_{x_i}\right)^2} \tag{23}$$
$$R = f\left(x_1, x_2, ..., x_n\right)$$

where R is the dependent variable, x_i is an independent variable and u_{xi} is the uncertainty of that independent variable. The uncertainty for the preliminary results is given as error bars in each plot. The uncertainty of each independent variable is dominated by the calibration error. The vertical error bars in the plots of the preliminary data represent the uncertainty for the y-axis variable and the horizontal error bars for the x-axis variable.

Preliminary Results

As discussed earlier, preliminary data were collected to measure the flow rate of extracted vapor as a function of extraction pressure differential and the pressure drop across the fractal piece as a function of inlet flow rate. The inlet subcooling was held constant at 2˚ C. The data collected for the first comparison are summarized in Fig. 12. In this set of data, the heat transferred from the heating coil to the microchannels was constant at 8.5 W (this is accounting for the calculated losses) and the inlet flow rate remained constant at 5 g/min. The flow rate linearly increases with extraction pressure differential between 13.8 to 34.5 kPa (2 - 5 psi). With an extraction pressure differential across the porous media greater than 34.5 kPa (5 psi), the flow rate of extracted vapor reaches a maximum and no longer increases. A better representation of vapor extraction is given in the secondary vertical axis where the percent of the flow extracted, m_{vap}/m_{in}*100, is given as a function of extraction pressure differential.

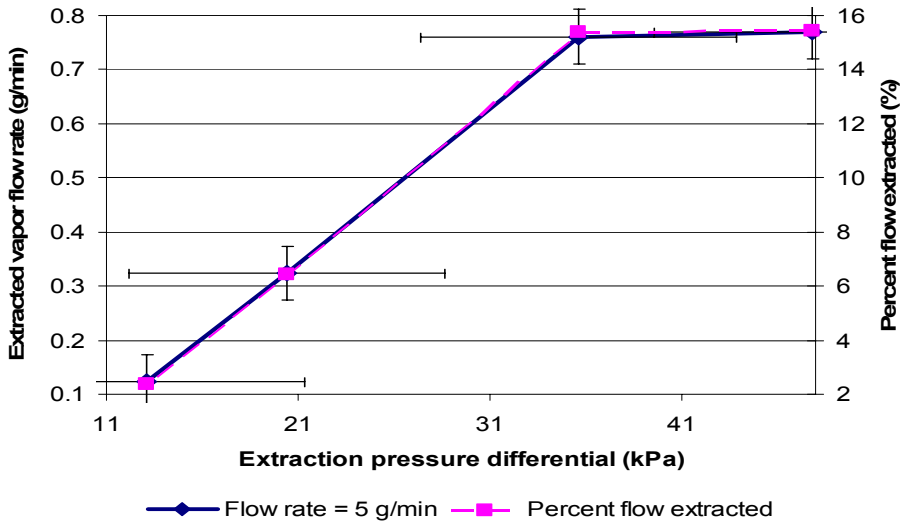

Figure 12: Flow rate of extracted vapor and percent flow extracted as a function of pressure differential across porous media with applied power and inlet flow rate held constant. The error bars represent the uncertainty in both variables.

To find the relationship between pressure drop across the microchannels and inlet flow rate, the applied voltage and extraction pressure differential are held constant at 8.4 V and 62 kPa (9 psi), respectively. Data were taken with inlet flow rates of 2, 3, 5, 6 and 9 g/min. The pressure drop increase as the inlet flow rate increases and this trend is shown in Fig. 13. A secondary vertical axis plots the inlet pressure as a function of inlet flow rate. The pressure drop across the fractal and the inlet pressure follow the same general trend line because the outlet pressure remained constant. In Fig. 14 it is shown that the percentage of the flow extracted increases as the pressure drop across the fractal piece decreases.

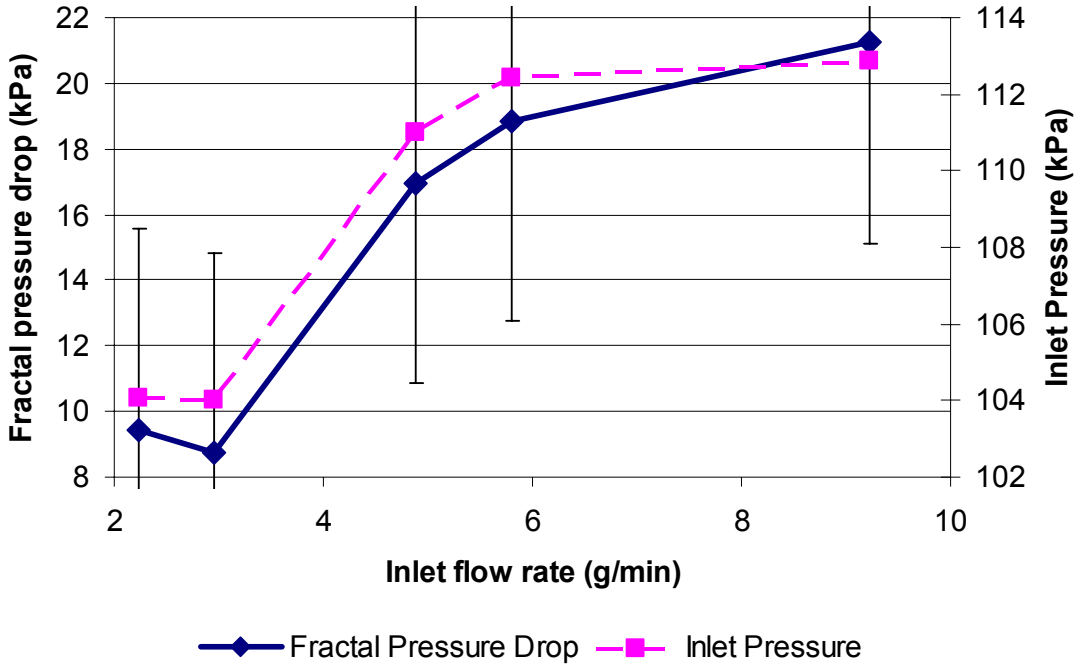

Figure 13: Pressure drop across fractal piece and inlet pressure as a function of inlet flow rate with the applied power and extraction pressure differential held constant. The error bars represent the uncertainty in both variables.

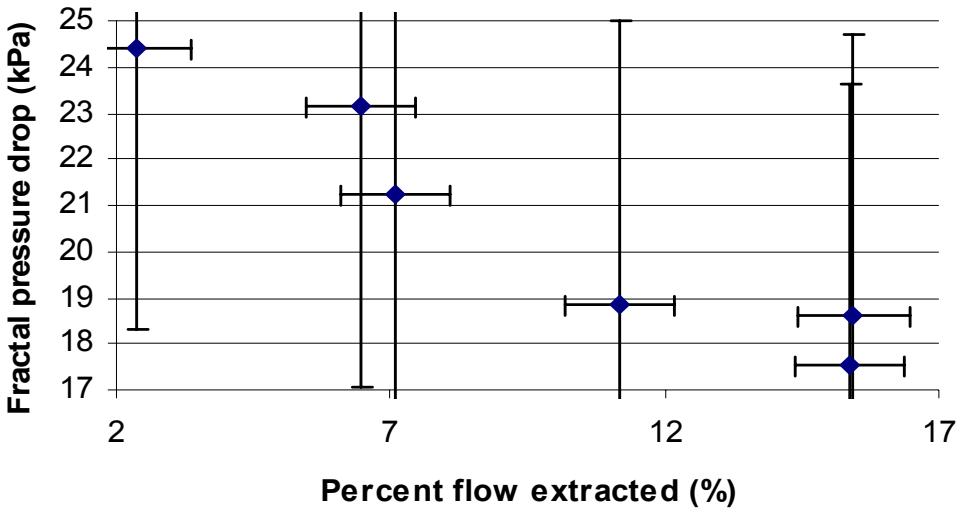

Figure 14: Pressure drop across fractal piece as a function of percentage of flow extracted with the applied power held constant. The error bars represent the uncertainty in both variables.

Conclusion and Recommendations

In conclusion, a test fixture was designed and fabricated that met the design requirements for the project. Around the test fixture, a flow loop was designed and constructed that facilitates experimental validation of the thesis statement. Preliminary data was collected and the results inconclusively support the thesis statement. The trend in Fig. 14 shows that as the percent of flow extracted increases the pressure drop across the heat sink decreases. The pressure drop across a pipe or any internal flow is directly proportional to the inlet flow rate. Consequently, extracting part of the flow reduces the pressure drop. Examining Fig. 14, it is determined that the reduction in pressure drop is due to both the reduced flow rate and the extraction of vapor. A maximum of fifteen percent of the flow is extracted in the preliminary data collection. If the vapor is immediately removed then the reduced pressure drop is proportional to the reduced flow rate—fifteen percent. However, if the vapor is removed at the exit, then the pressure drop is not reduced. In this project, the vapor is not removed entirely at the inlet or the exit of the microchannels. Assuming that the vapor is extracted evenly throughout the flow, the reduction in pressure drop due solely to reducing the flow rate is approximately half the percent of flow extracted. In Fig. 14, the pressure drop is reduced from 25 to 18 kPa by extracting 15% of the flow. Using the above assumption, 7% or 1.75 kPa of the reduction is due to the reduced flow rate and the remaining 5.25 kPa reduction in the fractal pressure drop is a consequence of locally extracting the vapor from the flow. Twenty-five percent of the reduction is due to reducing the flow rate. Local extraction of the vapor minimizes the effect of local acceleration of the flow due to the formation of

vapor and reduces the heat sink pressure drop by seventy five percent. Once modifications are made, more data will be collected to better quantify the effect of vapor extraction on microchannel heat sink performance.

It is expected that as the flow rate increases the pressure drop across the fractal increases. The results in Fig. 13 in general follow the expectation. However, the vapor plenum pressure, not the extraction pressure differential, was kept constant in this analysis. Data needs to be collected with the extraction pressure differential kept constant. It is expected that this will result in data that more clearly follows the expectations.

A maximum of 0.75 g/min or 15% of the flow is extracted (see Fig. 12) when the input energy, subcooling and flow rate remained constant. It is not clear what the implications of this maximum are. Under ideal conditions, conservation of mass would indicate the amount of vapor that passed through the microchannels. Large fluctuations in the output of the mass flow meter measuring the outlet liquid flow rate do not make this analysis possible. The testing procedure will be improved to produce reliable readings on the flow rate of the exiting liquid.

Most of the design requirements of the fixture and test loop were met, but there remain a few unresolved issues with the test fixture and flow loop. The small vacuum tight Upchurch fittings did not work as desired and so it is recommended that different fittings be used. In creating the differential pressure for vapor extraction, the catch basin (a polypropylene bottle) for the condensed vapor would change volume resulting in fluctuations in the mass balance readings. To remedy this problem, a rigid container (preferably made of glass) will be used to catch the condensation. Improvement also

needs to be made to the heater block design. The coiled groove in the original heater block is too tightly spaced and does not provide sufficient cross-sectional area remaining for vapor extraction. Another heater block will be designed with a 1.59 mm (1/16 in.) groove, instead of a 3.18 mm (1/8 in.) groove, and its radius of curvature will be increased to provide more area for vapor extraction. The new heater design also increases the length of coiled wire resulting in a greater heater resistance.

After the improvements are made, data collection will continue. The testing procedure will include measurement of the extracted vapor flow rate as a function of extraction pressure differential for inlet flow rates ranging between 2 and 15 g/min. These sets of data will be collapsed into dimensionless form to compare the fraction of flow extracted as a function of extraction pressure differential. Data will also be collected to find the effect of varying the input heat to the fractal network. All of this data will be compared to similar flow conditions without vapor extraction in order to validate the positive effect of vapor extraction on the microchannel heat sink.

References

1. E. M. Sparrow, J.E. Niethammer, and A. Chaboki, Heat transfer and pressure drop characteristics of array of rectangular modules in electronic equipment, *International Journal of Heat and Mass Transfer*, vol. 25, pp. 961-973 (1982).

2. B.A. Jubran, S. A. Swiety, and M.A. Hamdan, Convective heat transfer and pressure drop characteristics of various array configurations to simulate the cooling of electronic modules, *International Journal of Heat and Mass Transfer*, vol. 39, pp. 3519-2529, 1996.

3. D. B. Tuckerman and R. F. W. Pease, High-Performance Heat Sinking for VLSI, *IEEE Electron Device Lett.*, vol. EDL-2, pp. 126-129, 1981.

4. W. Qu and I. Mudawar, Experimental and numerical study of pressure drop and heat transfer in a single-phase micro-channel heat sink, *International Journal of Heat and Mass Transfer*, vol. 45, pp. 2549-2565, 2002.

5. L. Zhang, S. S. Banerjee, J. Koo, D.J. Laser, M. Ashegi, K.E. Goodson, J. G. Santiago, and T.W. Kenny, A micro heat exchanger with integrated heaters and thermometers, *Proceedings of Solid State Sensor and Actuator Workshop*, pp. 275-280, June 2000.

6. R. Mertz, A. Wein, and M. Groll, Experimental investigation of flow boiling heat transfer in narrow channels, *Second European Thermal Sciences and 14th UIT National Heat Transfer Conference*, Rome, May 26-31, 1996.

7. W. Qu and I. Mudawar, Measurement and prediction of pressure drop in two-phase micro-channel heat sinks, *International Journal of Heat and Mass Transfer*, vol. 46, pp. 2737-2753, 2003.

8. M. E. Steinke and S. G. Kandlikar, An Experimental Investigation of Flow Boiling Characteristics of Water in Parallel Microchannels, *Journal of Heat Transfer*, vol. 126, pp. 518-526, 2004.

9. L. Jiang, M. Wong, and Y. Zohar, Forced Convection Boiling in a Microchannel Heat Sink, *Journal of Microelectromechanical Systems*, vol. 10, pp. 80-87, 2001.

10. L. Zhang, J. Koo, L. Jiang, M. Ashegi, K. E. Goodson, J. G. Santiago, and T. W. Kenny, Measurement and Modeling of Two-Phase Flow in Microchannels with Nearly Constant Heat Flux Boundary Conditions, *Journal of Microelectromechanical Systems*, vol. 11, pp. 12-19, 2002.

11. H. H. Bau, Optimization of Conduits' Shape in Micro Heat Exchangers, *International Journal of Heat and Mass Transfer*, vol. 41., pp. 2717-2723, 1998.

12. G. B. West, J. H. Brown, and B. J. Enquist, A General Model for the Origin of Allometric Scaling Laws in Biology, *Science*, vol. 276, pp. 122-126, 1997.

13. D. V. Pence, Improved Thermal Efficiency and Temperature Uniformity using Fractal-like Branching Channel Networks, *Proceedings of the International Conference on Heat Transfer and Transport Phenomena in Microscale*, ed. G.P. Celata, Begell House: New York, pp. 142-148, 2000.

14. D. V. Pence, Reduced Pumping Power and Wall Temperature in Microchannel Heat Sinks with Fractal-like Branching Channel Networks, *Microscale Thermophysical Engineering*, vol. 6, pp. 319-330, 2002.

15. D. V. Pence and K. Enfield, Inherent Benefits in Microscale Fractal-like Devices for Enhanced Transport Phenomena, *Design and Nature II: Comparing Design in Nature with Science and Engineering*, WIT Press, pp. 1051-1057, 2004.

16. W. Qu and I. Mudawar, Flow boiling heat transfer in two-phase micro-channel heat sinks—I. Experimental investigation and assessment of correlation methods, *International Journal of Heat and Mass Transfer*, vol. 46, pp. 2755-2771, 2003.

17. T. H. Yen, N. Kasagi, and Y. Suzuki, Forced Convective Boiling Heat Transfer in Microtubes at Low Mass and Heat Fluxes, *Symposium on Compact Heat Exchangers on the 60th Birthday of Ramesh K. Shah*, pp. 401-406.

18. M. Ikeuchi, T. Yumikura, M. Fujii and G. Yamanaka, Heat-transfer characteristics of an internal micro-porous tube with refrigerant-22 under evaporating conditions, *ASHRAE Transactions*, vol. 90, pp. 196-211, 1984.

19. C. N. Ammerman and S. M. You, Enhancing Small-Channel Convective Boiling Performance Using a Microporous Surface Coating, *Journal of Heat Transfer*, vol. 123, pp. 976-983, 2001.

20. F. P. Incropera and D. P. DeWitt, *Fundamentals of Heat and Mass Transfer*, 5th ed., John Wiley & Sons, New York, NY, pp. 490, 2002.

21. A. Y. Alharbi, D. V. Pence and R. N. Cullion, Fluid Flow Through Microscale Fractal-like Branching Channel Networks, *Journal of Fluids Engineering*, vol. 125, pp. 1051-1057, 2003.

APPENDIX A

Design Specification Calculations

Preheating Tube Length Calculations:

Calculations determining the length of aluminum tubing in the hot oil bath needed to preheat the inlet flow are done in this section. The equations governing this length are found in the Design Specifications section. A high flow rate of 15 g/min (2.5E-4 kg/s) is examined to establish the upper limit of the required length. The Reynold's number of the flow is calculated to verify that it is in the laminar region using

$$\mathrm{Re}_D = \frac{UL}{\upsilon} = \frac{4\dot{m}}{\pi D_i \mu} \tag{1.A}$$

where D_i is the inner diameter of the tube (4.572 mm) and μ is the dynamic viscosity of water evaluated at the mean temperature (~65˚ C) or 4.463E-4 kg/ms. The Reynolds number of the flow is 156 indicating the flow is laminar. The assumption that the flow is undeveloped within the oil bath is validated using the following correlation for laminar entrance length:

$$L_e = 0.06\,\mathrm{Re}\,D_i \tag{2.A}$$

The entrance length is calculated to be 4.3 cm. Signifying that after each bend in the tubing or transition through a fitting the flow has a developing velocity profile region. Consequently, due to the layout of the tubing in the oil bath the flow has an undeveloped velocity profile. As mentioned earlier, an iterative process is done to find the needed length. An initial guess is made for the length and then the Nusselt number and average heat transfer coefficient values are calculated. A length is calculated from these values and compared to the initial guess. If the guess is equal to the calculated value, then the process is complete. If there is a discrepancy in the values, then the calculated value helps determine the next guess and so forth. Table 1.A details this iterative process using Eqs. 4, 5 and 6 where the property values are taken at the mean temperature, the dynamic viscosity evaluated at the surface is 1.54E-4 kg/ms, the inlet mean temperature is assumed to be 24˚ C, the outlet mean temperature is 104˚ C, and the log mean temperature difference is 106.02 K where the temperature of the bath is set at 175˚ C.

Table 1.A: Iterative calculations performed to find length of tubing in hot oil bath.

Assumed L (cm)	$\overline{Nu}_D$	$\overline{U}$ (W/m^{2}K)	Calculated L (cm)
10	6.03	624.2	6.4
6.4	7.00	724.6	5.5
5.5	7.37	762.9	5.2
5.2	7.50	776.4	5.1
5.1	7.56	782.5	5.1

The length is found to be 5.1 cm. The bends in the tube ensure that the flow is undeveloped which decreases the length needed by improving the heat transfer rate. Similar calculations performed for developed flow indicate that 18.5 cm of tube are needed. The amount of tubing in the hot oil bath is increased to 30 cm to insure that the

desired outlet temperature is achieved. The temperature of the hot oil bath can be adjusted to achieve the appropriate preheating.

The same procedure can be used to calculate the temperature that the bath should be maintained at as a function of the mass flow rate. The same property values are used and the unknown variable is now the constant surface temperature. Table 2.A lists the temperature at which to maintain the hot oil bath for a series of flow rates.

Table 2.A: Recommended oil bath temperature as a function of inlet flow rate.

Inlet flow rate (g/s)	Oil Bath Temp. (˚ C)
2 – 7	106
8 – 9	107
10 – 11	108
12 – 13	109
14 – 15	111

Percentage of Heat Transferred to Microchannels:

The percentage of heat that is transferred to the flow in the microchannels is approximated using a thermal circuit analysis. Figure 6 schematically represents how this approximation is made. The top branch R_{ncv} represents the natural convection of heat to the air above the heater and R_{rad} is the radiation of heat to the surrounding air. The heat transfer coefficient for natural convection is found using the Rayleigh number and the Nusselt number:

$$Ra = \frac{gB(T_s - T_\infty)L^3}{\upsilon\alpha} \tag{3.A}$$

$$\overline{Nu}_L = 0.54Ra^{0.25} \tag{4.A}$$

where g is the acceleration due to gravity, B is the inverse of the mean temperature (1/350K), T_s is the surface temperature (125˚ C), T_∞ is the surrounding temperature (25˚ C), υ is the kinematic viscosity (20.92E-6 m^2/s), and α is the thermal diffusivity (29.9E-6 m^2/s). The fluid properties are calculated at the mean temperature. The natural convection thermal resistance is then calculated using Eqs. 8c and 6 (substituting U for h) as approximately 13,400 K/W. The heat transfer coefficient for thermal radiation can be calculated using the following relationship:

$$h_{rad} = \varepsilon\sigma(T_s + T_\infty)(T_s^2 + T_\infty^2) \tag{5.A}$$

The same two temperature values are used and ε is the emissivity of the wire (approximately 0.8) and σ is Boltzman's constant (5.67E-8 W/m^2*K^4). The thermal resistance of the radiation is calculated using Eq. 8c and is equal to approximately 126.5 K/W. The three thermal resistances—$R_{s,al}$, $R_{s,peek}$, $R_{s,air}$—in the second branch are calculated using Eq. 8b, where the shape factor is

$$S = \frac{2\pi L}{\cosh^{-1}\left(\frac{D^2 + d^2}{2Dd}\right)} \tag{6.A}$$

This represents the two-dimensional conduction from a cylinder to a larger concentric cylinder. The two diameters represent the inner and outer diameter of the larger cylinder. The effective thermal resistance of the middle level is 862 K/W. The branches representing lost heat can be considered to be parallel as depicted in Fig. 6 and the effective thermal resistance of these branches is then calculated as 110 K/W using the relationship

$$\frac{1}{R_{loss}} = \frac{1}{R_{ncv}} + \frac{1}{R_{rad}} + \frac{1}{R_{s,al} + R_{s,peek} + R_{s,air}} \tag{7.A}$$

Similar to electrical circuits, if the potential across a resistor is known then the current passing through the resistor is easily calculated using Ohm's law. In this case, the heat loss is calculated using the thermal equivalent of Ohm's law:

$$\dot{q}_{loss} = \frac{T_s - T_\infty}{R_{loss}} \tag{8.A}$$

The heat loss is calculated to be approximately 1 W.

Verification of Complete Condensation of Extracted Vapor:

It is important to verify that the extracted vapor is completely condensed before exiting the cold water bath. If it does not completely condense, then the vapor may pass through the catch system and exit to the atmosphere via the vapor pump. This analysis is similar to that done for the preheating calculations. In this case, the inlet temperature, outlet temperature and surrounding temperature are 115, 95 and 25 ˚C, respectively. The length of tubing is 0.45 m (18"). To avoid the complications of latent heat exchange and simply verify complete condensation, the heat transferred away from the flow is compared to that which is required to condense the flow. The heat transferred from the flow is given by Eq. 1 and the minimum heat that must be transferred is given by Eq. 3. Assuming a maximum vapor flow rate of 3 g/min (20 percent of a maximum inlet flow rate of 15 g/min) and evaluating properties at 380 K (107 ˚C), the required heat transfer from the system to condense the flow is 2 W. With the Reynold's number determined using Eq. 1.A, the Nusselt number is calculated as 5.08 using Eq. 5. From the definition of the Nusselt number in Eq. 6, the average heat transfer coefficient is calculated to be 13.2 W/m^2K. The heat transferred from the vapor flow to the cold bath is 14.4 W. More than seven times the required heat is transferred from the vapor flow to the water bath in order to completely condense the extracted vapor.

APPENDIX B

Pictures of Test Fixture and Flow Loop

Figures 1.B – 5.B are pictures of the test loop and test fixture. In Fig. 1.B, bare stainless steel tubing enters the hot oil bath. The preheated liquid exits the bath and the line is insulated to minimize heat losses. The fluid then enters the test fixture. The other insulated lines shown in the figure are part of an existing ammonia desorber flow loop. The water supply tank (clear tank in the bottom left), surge tank (grey) and the bladder tank (white) are shown in Fig. 2.B. The black pump draws water from the supply tank to the bladder tank which is pressurized by the surge tank. The catch and weigh system for the extracted vapor is shown in Fig. 3.B. The vapor is condensed in the cold bath and flows into the bottle on top of the scale. The small pressure station provides the vacuum pressure across the porous media. The scale is connected to the serial port of the nearby computer and the mass of the catch system is monitored and recorded. The tank pictured in this figure is the reservoir for the liquid and vapor that pass through the microchannels. Figure 4.B shows part of the test loop and how it is integrated with the existing flow loop. The water enters the flow loop from the bottom left and passes through an in-line filter before reaching the first three-way shut-off valve (left edge of figure). The temperature, pressure and mass flow rate are then measured for the inlet flow. After the regulatory needle valve, the flow loop diverges at the second three-way valve. The transducers used to measure the temperature, pressure and flow rate of the exit flow are shown in the right edge of the figure. The test fixture with the inlet and exit flow lines and its transducers are shown in Fig. 5.B.

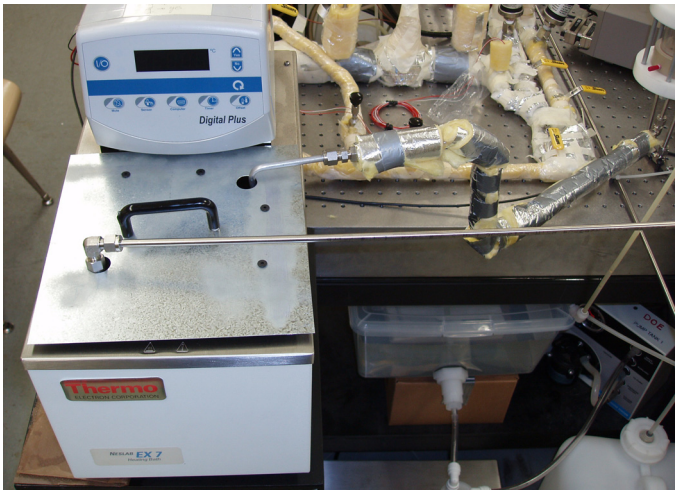

Figure 1.B: Picture of inlet flow entering and exiting hot oil reservoir to be preheated.

Figure 2.B: Picture of supply tank (clear), bladder tank (white) and surge tank (grey).

Figure 3.B: Catch and weigh system used to measure flow rate of extracted vapor including liquid collector and vapor pump.

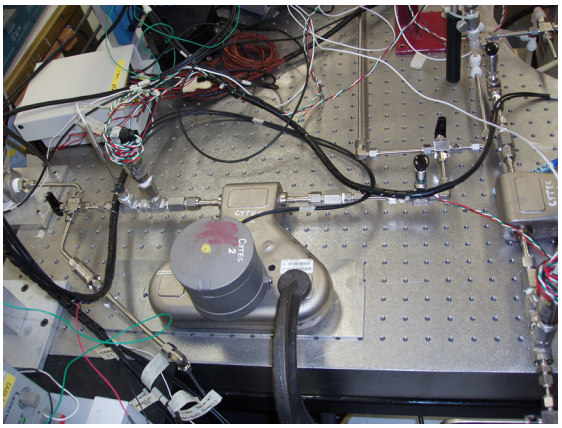

Figure 4.B: Transducers used to measure the temperature, pressure and flow rate of the inlet and exit flow lines.

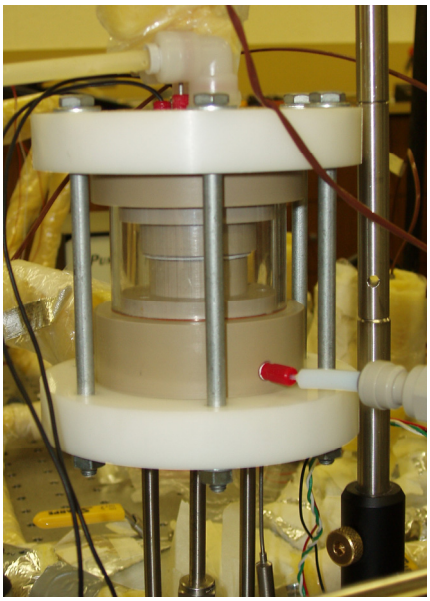

Figure 5.B: Test fixture with flow lines and its transducers to measure the needed flow properties.

APPENDIX C

Detail Drawings of Test Fixture Parts

This appendix contains detail drawings of the parts of the fixture and the fixture assembly generated in Solid Works. Dimensions for the parts are provided on the drawings and references are made to indicate placement of o-rings, tap sizes, etc. Figure 1.C is the drawing for the clamp parts used to tightly enclose the assembly. The Top part through which the flow enters the microchannels and around which bottom clamp is attached is found in Fig. 2.C. The center hole is for the inlet flow and the two outer holes serve to drain the excess water from the fixture. The Porous Aluminum part serving as the heating block and porous medium is included in Fig. 3.C. The path of the embedded heating wire is outlined by the traced line. Figure 4.C details the Bottom part through which the vapor is extracted. The five small ports are for two lead wires for the heating element, a thermocouple, and a pressure transducer. An extra small port is provided if needed for additional measurements. The port towards the end is the excess vapor exit. The Encasing part in Fig. 5.C encloses a small volume for the exit liquid and excess vapor.

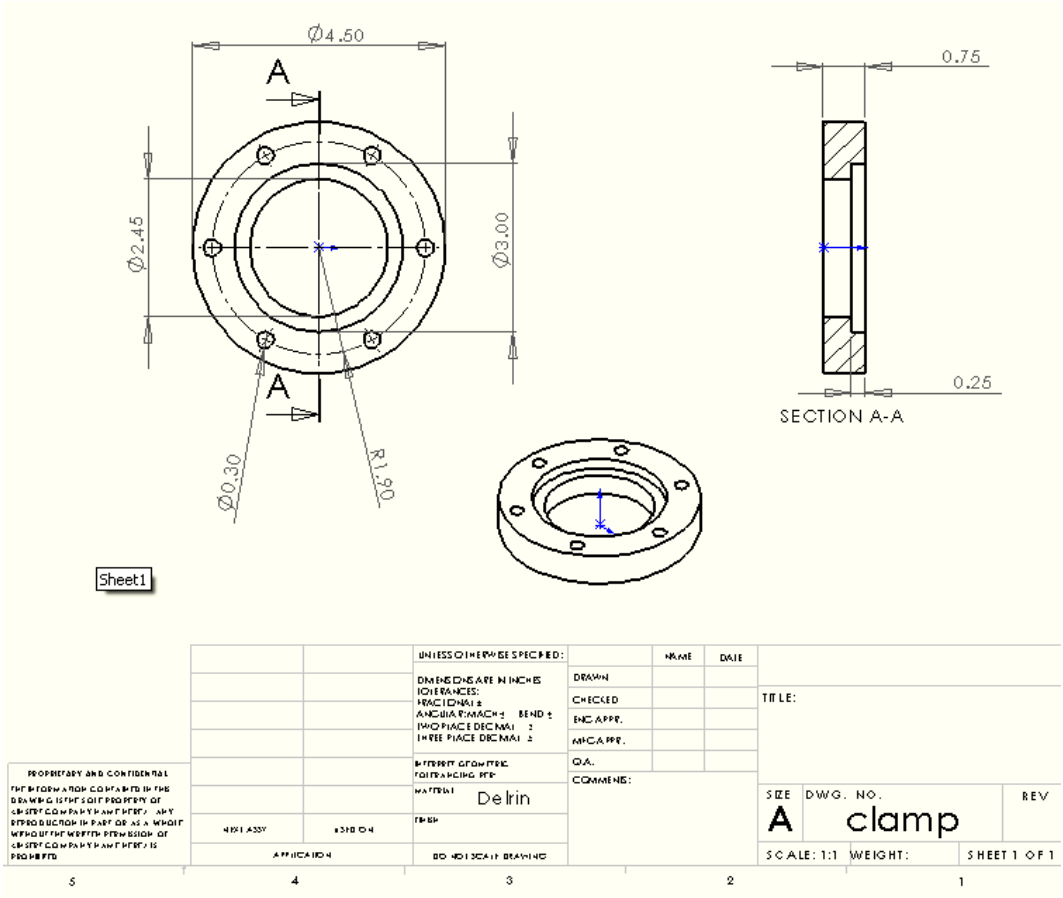

Figure 1.C: Drawing of the clamp enclosing the entire assembly.

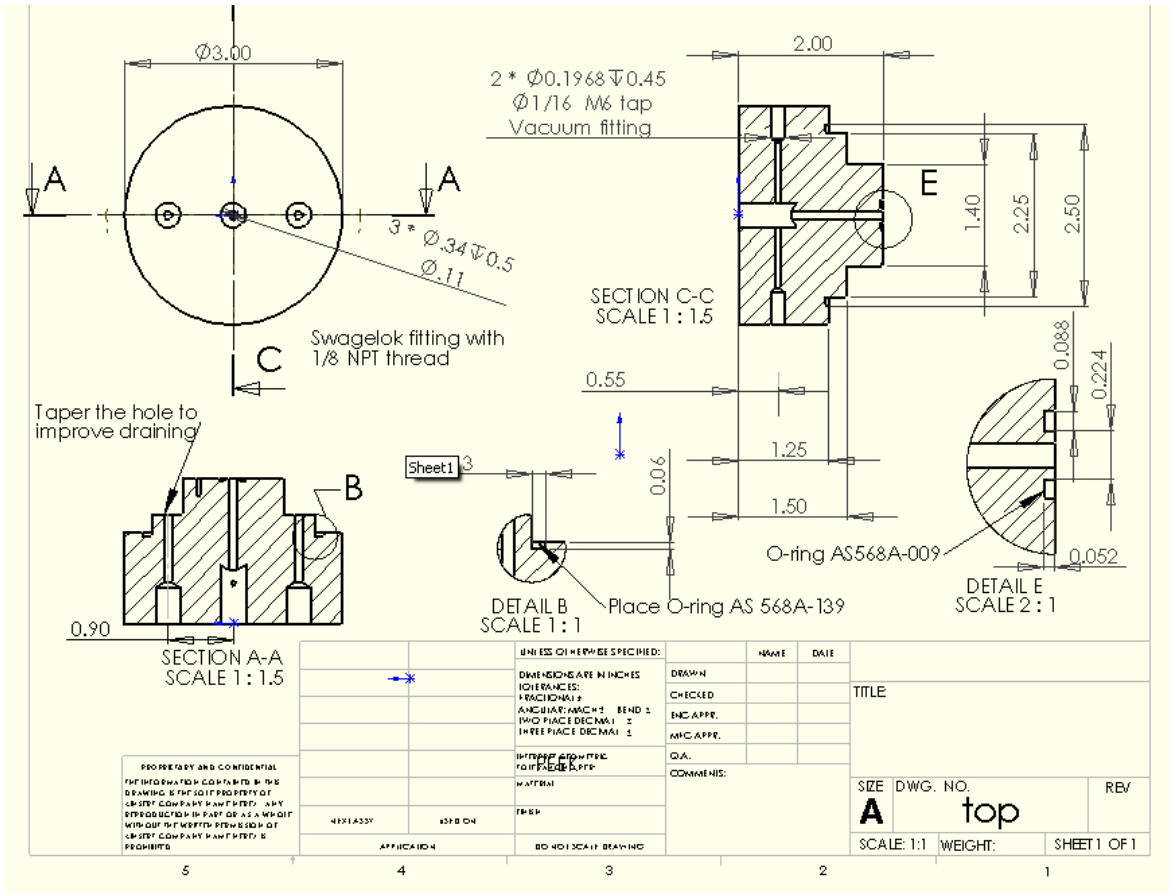

Figure 2.C: Top piece of fixture through which water enters the fractal. Ports for the inlet flow and excess water.

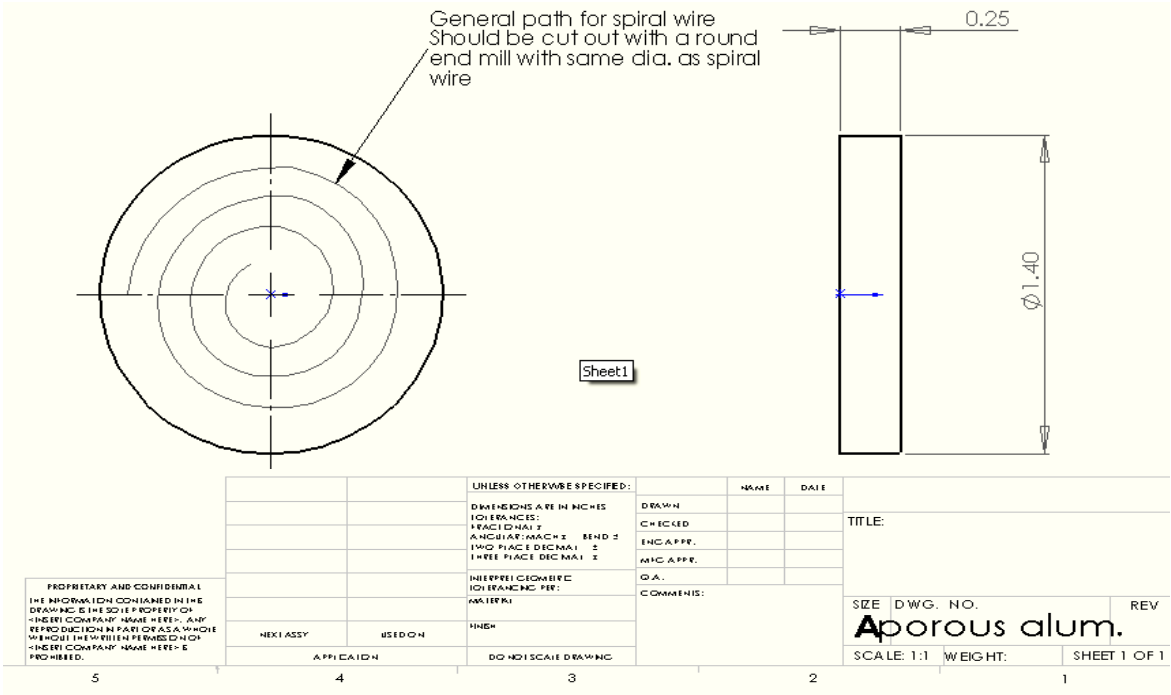

Figure 3.C: Porous aluminum layer with path of embedded wire shown.

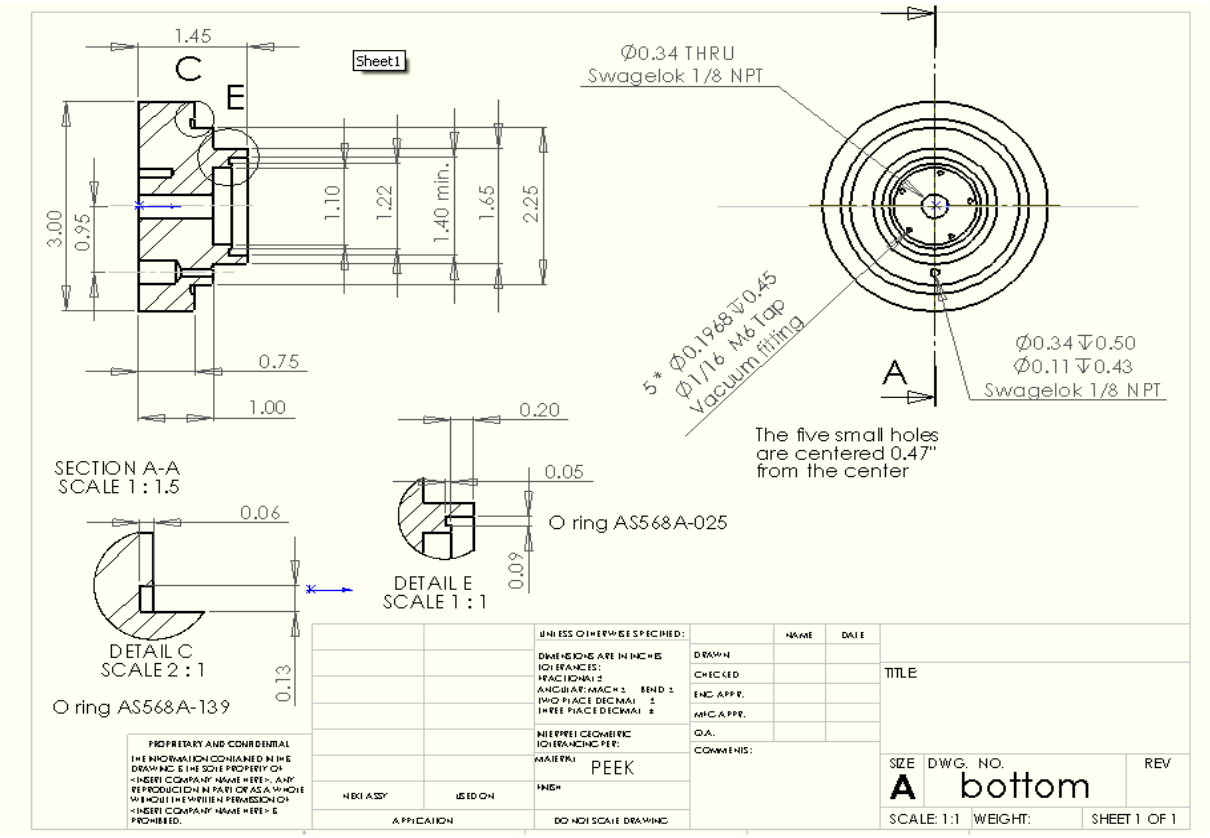

Figure 4.C: Bottom piece with five small ports, extracted vapor port and a port for the excess vapor.

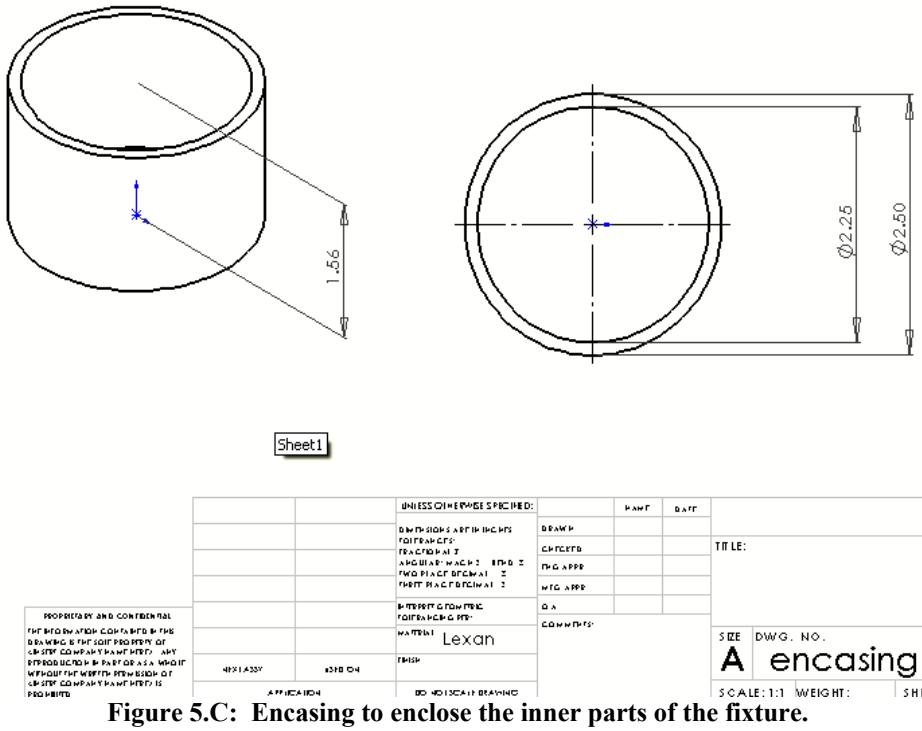

Figure 5.C: Encasing to enclose the inner parts of the fixture.

APPENDIX D

Calibration and Uncertainty for the Measurement Devices

The calibration curve, uncertainty, and range for each measurement device are given in Table 1.D. The calibration or curve fit for each device was found in a manner similar to that explained for in the Data Reduction and Analysis section of this thesis. In the curve equations, V is the output voltage from the device read by the computer and f is the frequency output by the mass flow meters. The scale was connected via the serial port and provided a direct digital output. The uncertainty values are calculated using Eq. 20. The uncertainty values are given as absolute values with the same units as indicated next to the device name. However, the uncertainty of the mass flow meters is given as a percentage of the output value. The uncertainty values are used as the bias error in the uncertainty calculations for the preliminary data. A range for each device is established by the manufacturer.

Table 1.D: Calibration curve, uncertainty, and range for each measurement device used in data collection.

Measurement Device	Calibration Curve	Uncertainty (±)	Range
P_{up} (kPa)	$P_{up} = 13470.9\ V_{up} - 28.122$	5.503*	0 – 1380
P_{in} (kPa)	$P_{in} = 2059.9\ V_{in} - 3.604$	3.548*	0 – 207
P_{out} (kPa)	$P_{out} = 105.95\ V_{out} - 6.273$	4.964*	0 – 414
P_{vac} (kPa)	$P_{vac} = 2050.83\ V_{vac} - 4.4708$	7.666*	0 – 207
T_{up} (˚C)	$T_{up} = 1\ V_{up} + 0.7894$	0.241*	-270 – 850
T_{in} (˚C)	$T_{in} = 1\ V_{in} + 2.1892$	0.211*	0 – 980
T_{out} (˚C)	$T_{out} = 1\ V_{out} + 2.1842$	0.213*	0 – 980
T_{vac} (˚C)	$T_{vac} = 1\ V_{vac} + 2.0227$	0.212*	0 – 980
$\dot{m}_{in}\ (g/\min)$	$\dot{m}_{in} = 0.065\ f_{in}$	0.116%#	0 – 1361
$\dot{m}_{out}\ (g/\min)$	$\dot{m}_{out} = 0.065 f_{out}$	0.103%#	0 – 1361
m_{vap} (g)	---	0.05#	0 – 11000

* Uncertainty includes both bias and curve fit errors associated with the measurement device.

\# Uncertainty is manufacturer provided bias error.